Aerial observations of the evolution of ice surface conditions during summer

D. K. Perovich, W. B. Tucker III, and K. A. Ligett

Engineer Research and Development Center–Cold Regions Research and Engineering Laboratory, Hanover, New Hampshire, USA

Received 17 May 2000; revised 15 January 2001; accepted 6 November 2001; published 26 October 2002.

[1] During spring and summer, the Arctic pack ice cover undergoes a dramatic change in surface conditions, evolving from a uniform, reflective surface to a heterogeneous mixture of bare ice, melt ponds, and leads. This transformation is accompanied by a significant decrease in areally averaged, integrated albedo. The key factors contributing to this reduction in albedo are the melting of the snow cover, the formation and growth of the melt ponds, and the increase in the open water fraction. To document these changes and enable quantification of the evolution of the ponds throughout the melt season, a program of aerial photography was carried out at the main site of the Surface Heat Budget of the Arctic Ocean (SHEBA) program. A modified square pattern, 50 km on a side, surrounding the SHEBA site was flown at altitudes ranging from 1220 to 1830 m. Twelve of these aerial survey photography flights were completed between 20 May and 4 October 1998. The flights took place at approximately weekly intervals at the height of the melt season, with occasional gaps as long as 3 weeks during August and September due to persistent low clouds and fog. In addition, flights on 17 May and 25 July were flown in a closely spaced pattern designed to provide complete photo coverage of a 10-km square centered on the SHEBA main site. Images from all flights were scanned at high resolution and archived on CD-ROMs. Using personal computer image processing software, we have measured ice concentration, melt pond coverage, statistics on size and shape of melt ponds, lead fraction, and lead perimeter for the summer melt season. The ponds began forming in early June, and by the height of the melt season in early August the pond fraction exceeded 0.20. The temporal evolution of pond fraction displayed a rapid increase in mid-June, followed by a sharp decline 1 week later. After the decline, the pond fraction gradually increased until mid-August when the ponds began to freeze. By mid-September the surface of virtually all of the ponds had frozen. The open water fraction varied between 0.02 and 0.05 from May through the end of July. In early August the open water fraction jumped to 0.20 in just a few days owing to ice divergence. Melt ponds were ubiquitous during summer, with number densities increasing from 1000 to 5000 ponds per square kilometer between June and August. *INDEX TERMS:* 4540 Oceanography: Physical: Ice mechanics and air/sea/ice exchange processes; 3360 Meteorology and Atmospheric Dynamics: Remote sensing; 3359 Meteorology and Atmospheric Dynamics: Radiative processes; *KEYWORDS:* sea ice, melt ponds, image processing

Citation: Perovich, D. K., W. B. Tucker III, and K. A. Ligett, Aerial observations of the evolution of ice surface conditions during summer, *J. Geophys. Res.*, *107*(C10), 8048, doi:10.1029/2000JC000449, 2002.

1. Introduction

[2] Results from general circulation models indicate that the Arctic sea ice cover should not only exert a strong influence on global climate, but also be a sensitive indicator of climate change [*Ingram et al.*, 1989; *Manabe et al.*, 1991; *Rind et al.*, 1995]. These results also indicate that there are considerable uncertainties regarding the treatment of the ice albedo and cloud radiation feedback mechanisms in such models. Because of ongoing questions about the specific role of such feedbacks in climate, a research program on the Surface Heat Budget of the Arctic Ocean (SHEBA) was initiated by the National Science Foundation in conjunction with the Office of Naval Research [*Moritz et al.*, 1993; *Moritz and Perovich*, 1996; *Perovich et al.*, 1999]. One of the central goals of the SHEBA program is to understand and quantify the sea ice-albedo feedback mechanism on scales ranging from meters to thousands of kilometers.

[3] The albedo of a sea ice cover depends upon the depth and state of the snow cover, the optical properties of the snow and ice, the properties and distribution of the melt ponds, and the amount of open water [*Zubov*, 1945; *Grenfell and Maykut*, 1977; *Grenfell and Perovich*, 1984; *Carsey*, 1985; *Barry et al.*, 1993; *Lindsay and Rothrock*, 1994; *Barry*, 1996; *Perovich et al.*, 2002; *Curry et al.*, 2002]. In sharp contrast to

the highly reflective ice, leads reflect less than 10% of the incident solar radiation and ponds only 20–40%. Solar energy absorbed in leads is the primary source of heat for bottom and lateral ablation [*Maykut and McPhee*, 1995]. How this energy is partitioned between lateral melting and bottom melting it is not well established, but is believed to depend on lead width and floe perimeter [*Maykut and Perovich*, 1987; *Steele*, 1992]. Pond-covered ice has a lower albedo than bare ice, experiences more melting [*Untersteiner*, 1961; *Hanson*, 1965], stores more solar energy, and transmits more solar energy to the ocean than bare ice. The key to understanding the ice-albedo feedback is to document physical processes that govern the state of the ice cover in response to forcing from the atmosphere and ocean.

[4] At the local scale, it is possible to relate changes in albedo and mass balance to physical processes affecting the state of the ice cover. A basic objective of SHEBA is to extend the understanding of the ice-albedo feedback from local scales to scales that would be useful for climate models. The evolution of the pond fraction and lead fraction are primarily responsible for changes in albedo during summer. General Circulation Models (GCMs) typically have spatial scales of hundreds of kilometers, and thus are limited to characterizing physical processes at these large scales. A key means of improving the treatment of sea ice in large-scale models would be to internally compute the albedo as a function of such surface conditions as ice, pond, and lead fraction [*Briegleb and Bromwich*, 1998; *Fetterer and Untersteiner*, 1998; *Curry et al.*, 2002]. However, at present there are limited observations and little quantitative understanding of how atmosphere and ocean forcing affects the summer evolution of ice surface conditions and albedo [*Moritz et al.*, 1993; *Moritz and Perovich*, 1996; *Fetterer and Untersteiner*, 1998]. To accurately simulate the ice pack and its interaction with the atmosphere and ocean, large-scale models must develop suitable ways to take these factors into account. A first step toward a better understanding and improved models is to determine, from observations, the evolution of ice surface conditions on the scale of a single grid cell (approximately 50 $\times$ 50 km).

[5] The local processes affecting albedo, and their spatial variability, were well documented in the SHEBA experiment [*Perovich et al.*, 2002]. To extend the scale of the local measurements of the evolution of the ice cover during the melt season, a program of aerial photography was carried out. The photographs documented the evolution of the regional ice cover: a pristine, homogeneous, snow covered, highly reflective surface in spring, a heterogeneous mixture of bare ice, ponds, and leads in midsummer, and then a return to freezing conditions and a uniform, snow covered surface in the fall. This paper presents an overview of the aerial photography program; details on the collection, processing, and analysis of the aerial photographs; results describing the relative areas of ice, ponds, and leads at a variety of scales; floe perimeter data; and a statistical characterization of the size distribution and shape of ponds.

2. Previous Work

[6] Because of the importance of leads and ponds to the summer heat budget of the ice cover, there have been numerous studies directed at determining lead and pond fractions. Lead fractions have been determined using satellite sensors. However, obtaining pond fractions from satellites has been problematic. Clouds cover the ice pack for much of the summer, severely constraining opportunities for visible imagery. Microwave sensors are limited by the relatively small size of melt ponds and degraded performance attributable to the pervasive surface water. Aside from satellites, observations of pond and lead coverage have been made on spatial ranges ranging from tens of meters to hundreds of kilometers. Cameras mounted on towers [*Langleben*, 1969], tethered balloons [*Derksen et al.*, 1997], helicopters [*Holt and Digby*, 1985; *Eicken et al.*, 1994; *Perovich and Tucker*, 1997; *Tucker et al.*, 1999] and aircraft [*Rothrock and Thorndike*, 1984; *Tschudi et al.*, 1997, 2001], and satellites [*Fetterer and Untersteiner*, 1998] have been used. Particular emphasis has been placed on the evolution of melt pond area fraction, number density, and size.

[7] Some studies provided snapshots of pond properties for a particular region and time. For example, *Eicken et al.* [1994] determined that average August pond fractions and sizes were 16% and 100 m^2 in 1991 and 19% and 140 m^2 in 1993 in the Eurasian sector of the Arctic, while *Perovich and Tucker* [1997] found late-July pond fractions of 12% in the Beaufort Sea. Other studies monitored the evolution of pond properties for short periods, or in a few cases for the entire melt cycle. *Derksen et al.* [1997] suspended a camera from a tethered balloon to monitor changes in pond fraction of first-year ice during the onset of melt. Over a 10-day period, there was a linear increase in pond fraction from 0.0 to a maximum value of 0.5. Studies of shore-fast, first-year ice indicate that shortly after snowmelt the pond fraction is nearly 1.0, followed by a decrease with time as horizontal and vertical drainage features develop [*Holt and Digby*, 1985]. Studies indicate that in general pond fractions on first-year ice are greater than those on multiyear ice [*Fetterer and Untersteiner*, 1998; *Naggar et al.*, 1998]. Results averaged over 10 summers of pond measurements made on multiyear ice in the central Arctic [*Nazintsev*, 1964] showed a seasonal evolution where pond fraction increased from June to July then decreased from July to August. *Fetterer and Untersteiner* [1998] determined time series of pond coverage in the central ice pack using satellite imagery. They found maximum pond fractions were 40–50% on flat first-year ice and 30% on deformed multiyear ice. Interestingly, pond fraction decreased with time on the multiyear ice and increased with time on the flat first-year ice.

3. Instruments and Techniques

[8] To document ice surface changes at the aggregate scale and quantify the evolution of the ponds throughout the melt season, a program of aerial photography was carried out at Ice Station SHEBA [*Perovich et al.*, 1999a], the experiment site of the SHEBA program. Between May and October 1998 more than a dozen helicopter survey flights were made (Table 1). The flights took place at approximately weekly intervals from mid-May through early October 1998, with occasional gaps as long as 3 weeks during August and September, due to persistent low clouds and fog. An instrument package was mounted, in a downward-looking orientation, on the back of the Canadian Coast Guard BO-105 helicopter's storage compartment (Figure 1a). It consisted of

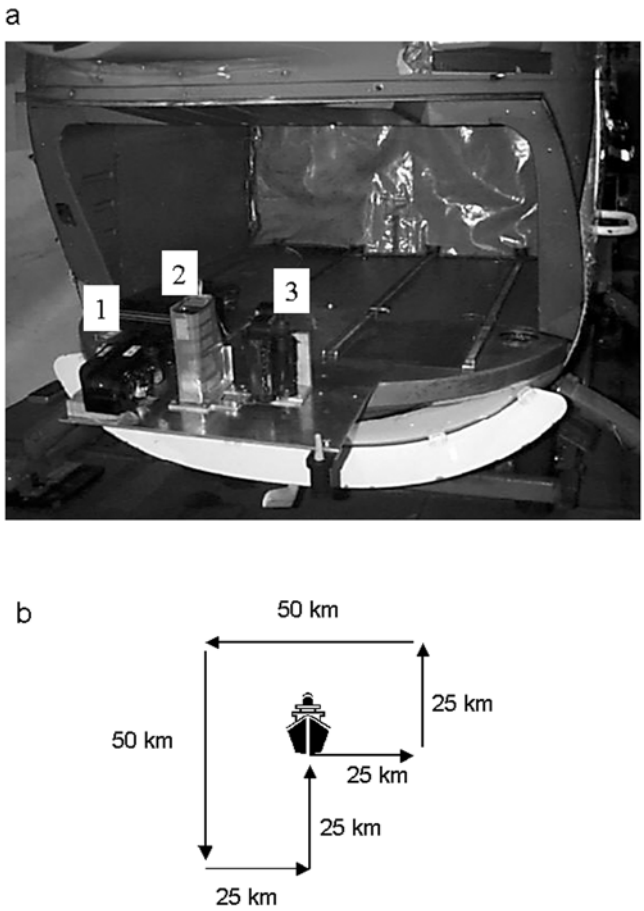

Figure 1. (a) Photograph of a fabricated plate protruding from the rear cargo compartment of a Canadian Coast Guard BO-105 helicopter holding (1) a Nikon 35-mm camera with a 250-frame film pack and motor drive, (2) a KT-19 thermal radiometer, and (3) a Hi-8 video camera. (b) A schematic of the standard aerial survey flight path.

a Nikon 35-mm camera equipped with a motor drive and 250-frame film roll, a Sony Hi-8 video camera, and a KT-19 thermal radiometer. Whenever possible, surveys were flown at an altitude of 1830 m under either clear skies or high clouds. At an altitude of 1830 m, each photograph covered an area of 1280 by 855 m (1.1 km^2). The flight pattern was a modified square pattern centered on the SHEBA site, as shown in Figure 1b. The first leg was 25 km east followed by 25 km due north, 50 km due west, 50 km south, then 25 km east, and finally 25 km north back to the ship. During each survey flight, approximately 200–250 color photographs were taken at regular intervals using the Nikon 35-mm camera. On most days, a 35-mm lens, an F-stop of 4.0, and a shutter speed of 1/1000 were used. On the survey flights, the photographs were spaced so that there was no overlap, and each photo was an independent sample. This flight path and photo spacing were selected to statistically estimate the surface characteristics for a GCM grid cell containing the SHEBA site. In addition to the surveys, flights on 17 May and 25 July were flown in a closely spaced pattern, designed to provide complete photo coverage of a 10-km square centered on the SHEBA main site.

[9] Negatives of the photographs were scanned using the Kodak Digital Science Photo CD process, which stores each image in several resolutions. A resolution of 1536 by 1024 pixels was used when determining the relative areas of different ice types. This gave a resolution of about 0.8 m per pixel for photographs taken from an altitude of 1830 m. A higher resolution (3072 by 2048 pixels, 0.4 m per pixel) was used when analyzing the size and geometry of ponds and floes. The complete set of aerial photographs is archived in a library of 36 CD-ROMs at the Joint Office for Scientific Support, Boulder, Colorado (http://www.joss.ucar.edu/cgi-bin/codiac/projs?SHEBA).

[10] The aerial photographs were processed using *Optimas* [1999], a commercial software package for personal computer-based image analysis. Each image was partitioned into its constituent components based on surface types, as outlined below. Figure 2 illustrates this by showing a sample image in original form (Figure 2a) and partitioned into ice, ponds, and leads (Figure 2b). Once an image was partitioned, the number of pixels in each category was counted and the fractional areas of the different surface types were calculated by dividing the number of pixels of a particular surface by the total number of pixels in the image. The area categories were snow covered and bare ice (A_i), ponded ice (A_p), newly formed young ice (A_y), and open

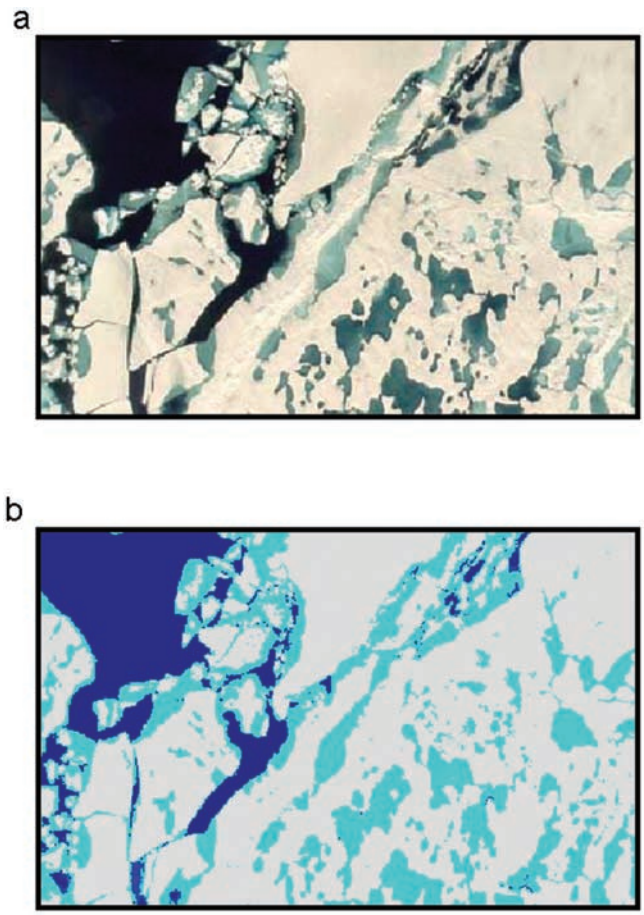

Figure 2. Aerial photograph from 20 July (a) before and (b) after partitioning into the constituent components of ice, ponds, and leads.

water (A_w), such that the sum of these four values is ideally equal to 1. For this study, the ice concentration is the sum of A_i and A_p.

[11] In May and early June, the surface consisted of two categories: snow covered ice and leads. Early in the melt season, melting snow was present in some areas, but this was difficult to distinguish optically from bare melting ice, as their albedos were similar [*Perovich et al.*, 2002]. From mid-June through mid-August, the surface was a mix of bare ice, ponded ice, and leads. Pond-like features were present at the edges of some regions of open water. These features typically resulted from lateral melting and edge erosion. In the fractional area analysis, these features are characterized as melt ponds because their optical properties are similar. Melt ponds that melted through appeared black and were optically similar to leads, and so were recorded as open water. Conditions were complex during fall freeze-up as leads and ponds began to freeze, and we considered ice, ponds, leads, and young ice. The young ice included new growth in both leads and in ponds.

[12] Partitioning of the images into the four surface categories was done by manually selecting color thresholds based on color-distribution histograms and on the image itself. Color was particularly useful in identifying the melt ponds, which typically had a bluish appearance. This process assumes that the RGB color thresholds for each feature type will be distinct and that there will be no overlap between threshold levels. The threshold levels for each surface category in each image were independently determined. As an indicator of threshold accuracy, the sum of the area percentages for each feature was nearly always within 2% of 100%; in fact, the data for many flights were consistently within half a percent of 100%. Once the fractional area per image of each feature type was calculated, results were normalized to total 100%. For each flight, the mean and the variance of the area fractions of the individual images were computed. Floe perimeter was determined by analyzing every fifth photograph for each flight.

[13] Some images could not be processed, because of poor contrast due to low clouds or fog. On images where the fog coverage was minimal and surface features were still visible and easily distinguished, PC-based photo-editing software was used to select leads by hand. In a few cases, images were converted from 24-bit RGB to eight-bit gray scale before partitioning to simplify the image partitioning and analysis.

[14] The National Imagery and Mapping Agency has released U.S. National Reconnaissance satellite images of the SHEBA area. The images, from SHEBA Reconnaissance Imagery Version 1.0, were obtained from the ARCSS Data Coordination Center, University of Colorado at Boulder [*National Snow and Ice Data Center*, 2000] (digital data available from nsidc@kryos.colorado.edu, Boulder, Colo.). We analyzed the first image released: a 57-km^2 photograph with approximately 1-m resolution that was centered on the ship and taken on 18 June 1998. These results are presented along with the data from the aerial photographs. Because satellite image was black and white, it was difficult to partition it to distinguish between melt ponds and leads. This difficulty was resolved by using Adobe Photoshop to "paint" the leads manually.

4. Results

[15] A qualitative understanding of the evolution of the ice cover can be gleaned from visually inspecting the aerial photographs. When survey flights were begun in May, the ice cover was relatively uniform. It consisted mainly of snow covered ice, with occasional freezing leads. A few days after the late-May start of the melt season, water began to collect in patches on the ice surface. Photographs from 10 June (Figure 3a) depict only a few light-colored, shallow ponds covering less than 2% of the surface. The ponds continued to spread, and by 22 June (Figure 3b) were ubiquitous. The early ponds were wide and shallow, and their perimeters were irregular and complex, paralleling small variations in ice surface topography. As the melt continued, ponds deepened; many of the shallow ponds drained into other, better-defined ponds.

[16] By early July, the ponds had formed distinct shapes. Throughout July they deepened and grew wider. As the ponds spread, they connected into large, complex networks. Quite a few ponds melted through to the ocean, which then accelerated their melting process (Figure 3c). *Zubov* [1945] noted that a few ponds melted through, and those were on ice that was less than 2 m thick. Given that SHEBA ice was relatively thin to start [*McPhee et al.*, 1998; *Perovich et al.*, 1999b] and that the summer melt season was long, it is not surprising that many ponds melted through.

[17] Ice Station SHEBA and its environs drifted as a Lagrangian tracer throughout the 13-month field experiment. From May through July, there was little divergence or deformation within the aerial survey region. Conditions changed dramatically, however, at the beginning of August after a period of sustained winds. There was divergence, a substantial increase in the amount of open water (Figure 3d), and significant relative motion among floes [*Richter-Menge and Perovich*, 2001].

[18] Fall freeze-up began in mid-August and by 22 August most of the ponds were covered by a thin layer of ice (Figure 3e). As freeze-up continued, most of the leads froze, and the ice surface was covered by a dusting of snow. By 4 October, the date of the last photography flight, there was ample young ice in leads and very little open water present (Figure 3f).

4.1. Area Fractions

[19] Area fractions were determined for nearly 2000 images covering more than 2050 km^2. Results from individual images along the flight line are plotted for 4 days in Figure 4. These days were selected to illustrate conditions when ponds first began to form (10 June), ponds quickly increased (22 June), pond and lead fractions were largest (7 August), and fall freeze-up was underway (4 October). There was considerable spatial variability along the path of each flight and between flights. The lead fraction rose and fell as the flight path crossed patches of open water and large floes. The pond fraction varied from photograph to photograph, and even within the same photograph. The graph for 10 June demonstrates the extreme variability of lead fraction on the scale of 1.1 km^2, the typical area covered by a single photograph. The increase in pond fraction on 22 June is striking. There was also significant spatial variability, with pond fractions varying by an order

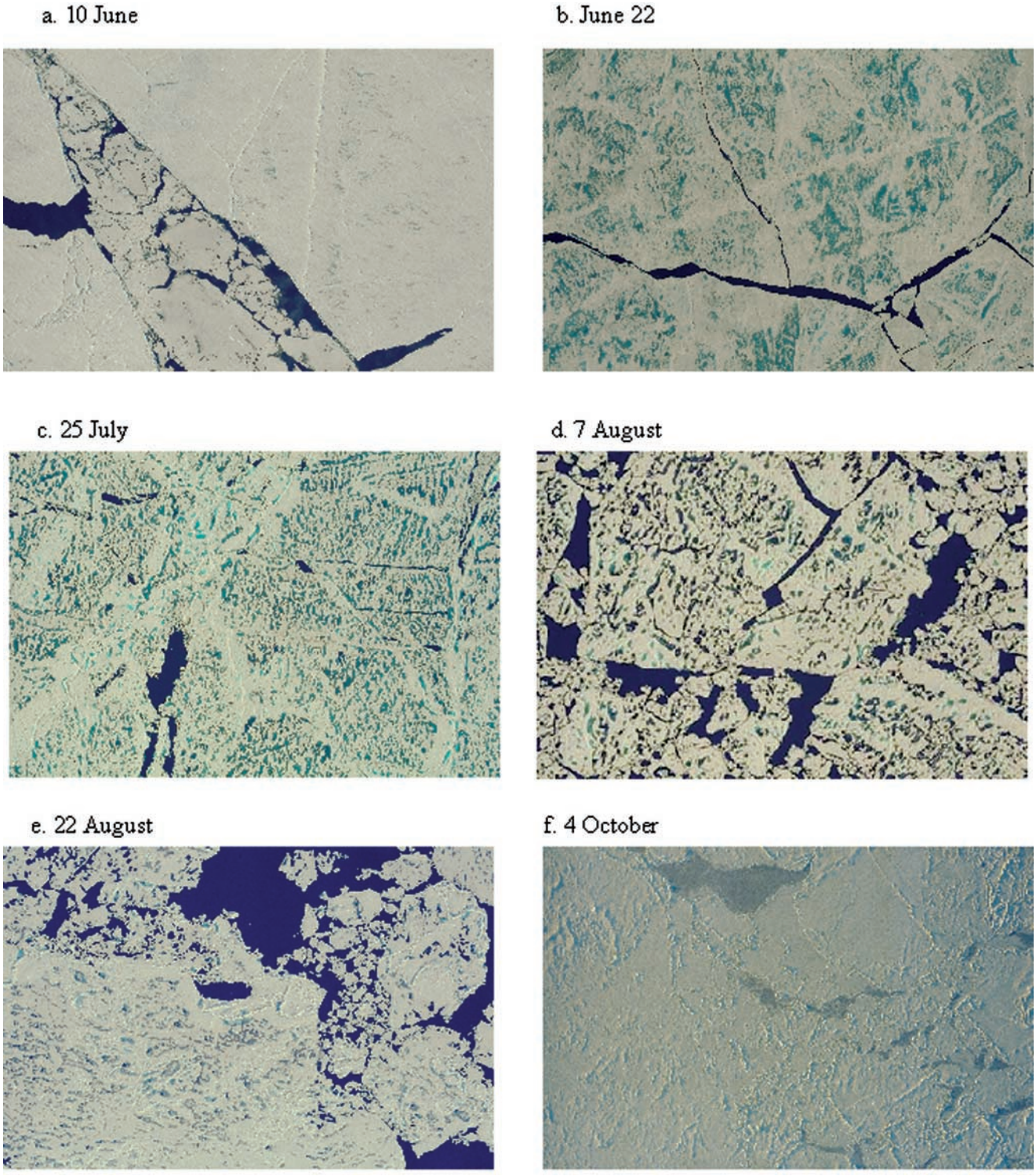

Figure 3. Photographs illustrating the dramatic changes that occur in the appearance of the ice cover before and after (a) onset of melt pond formation, (b) pond spreading, (c) pond evolution, (d) increase in the amount of open water due to divergence, (e) start of fall freeze-up, and (f) fall freeze-up.

of magnitude from 0.05 to 0.5. The large increase in open water fraction on 7 August is evident, as is the variability in lead fraction, which ranged from 0.05 to 0.9. By 4 October, the ponds were frozen and snow covered and were no longer distinguishable. Most of the leads were covered by young ice. There were extreme variations in young ice fraction 0.0 to almost 1.0 for image areas of 0.75 km^2.

[20] The average values of area fraction for a flight are the quantities of prime interest for extrapolating from the local scale, and for doing discrete element modeling or

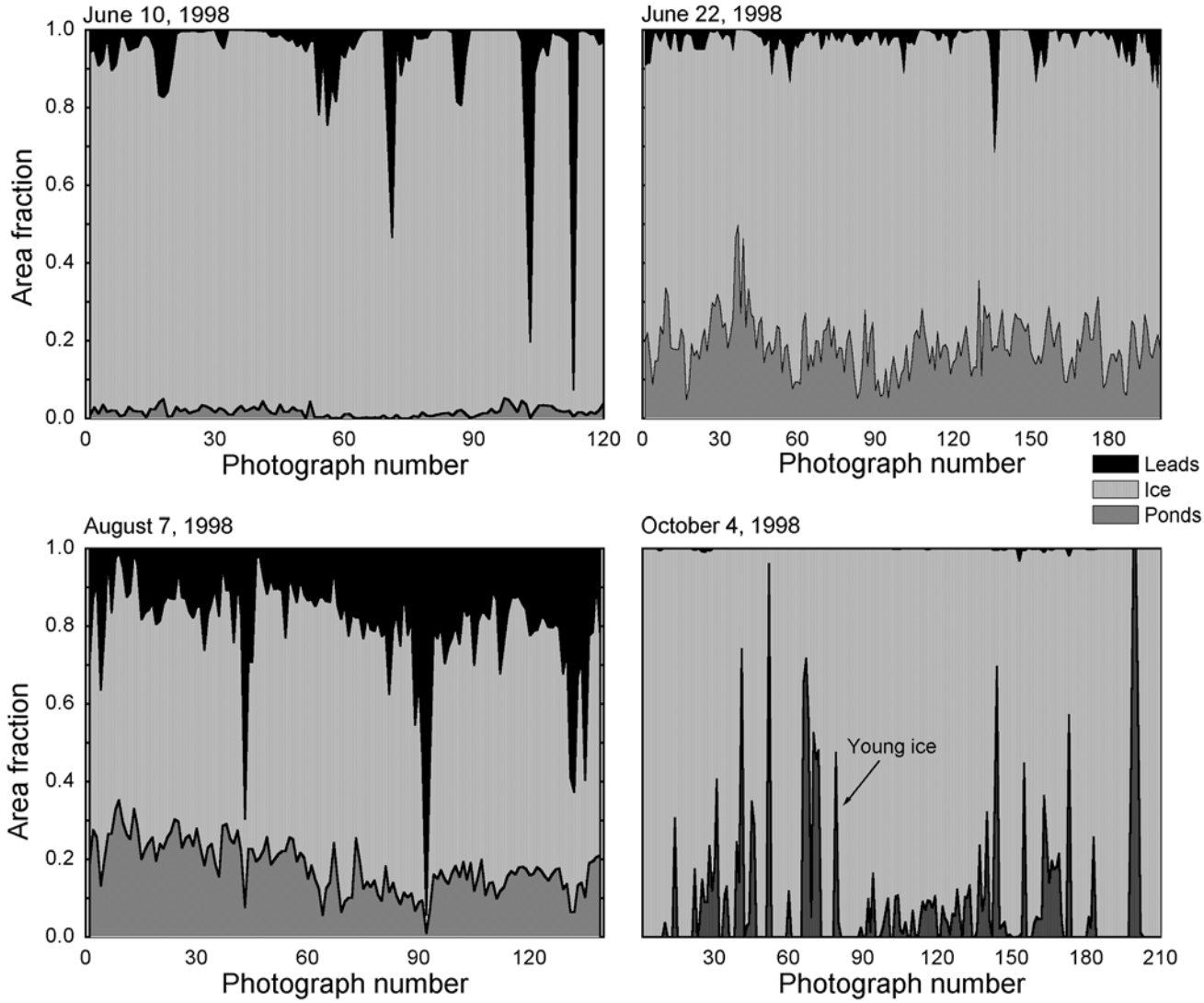

Figure 4. Area fractions of ice, ponds, and leads along the aerial survey flight path on (a) 10 June 1998, (b) 22 June 1998, (c) 7 August 1998, and (d) 4 October 1998.

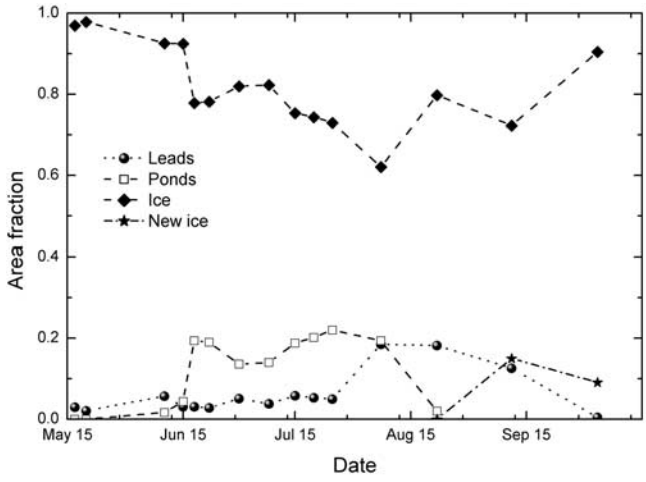

Figure 5. Average values of relative areas of ice, ponds, and leads from May 1998 through October 1998. Over 100 photos were analyzed for each flight.

single column modeling. The average area fractions for each day are plotted in Figure 5 and summarized in Table 1. Figure 5 shows the overall evolution of the ice cover surface conditions sampled along a 50- × 50-km box. This evolution is consistent with our qualitative observations. In May the surface was dominated by snow covered ice (0.98) with just a few leads (0.02). By mid-June ponds were extensive, resulting in a drop in ice fraction (0.78) and an increase in pond fraction (0.20). The ice fraction continued decreasing to 0.73 (25 July) as the ponds developed and matured. The early August divergence event caused a sharp, rapid drop in ice fraction to 0.62. Finally, as the leads and ponds begin to freeze in fall, the ice fraction increased to 0.90.

[21] Pond and lead fractions are plotted on an expanded scale in Figure 6 to accentuate their temporal dependence. Also plotted is the fraction of the ice that is ponded ($A_p^* = A_p/(A_i + A_p)$). This adjusts the pond fraction to account for changes due to variations in ice concentration. From mid-May through the end of July, lead fractions fluctuated in an unsystematic fashion between 0.02 and 0.05. At the beginning of August, in just a few days, there was a four-fold

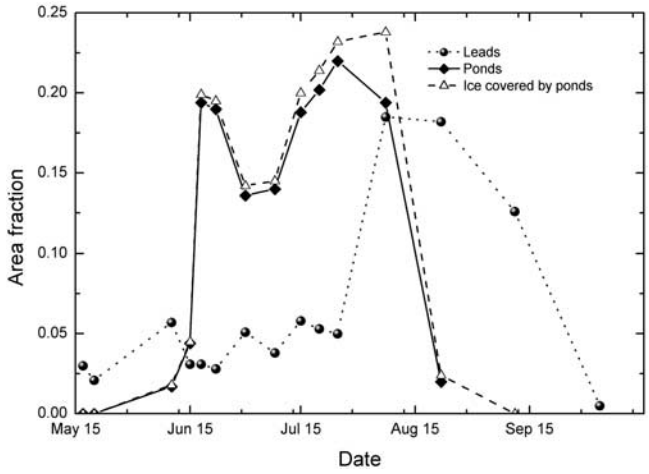

Figure 6. Time series showing fraction of the total area covered by ponds and leads, and the fraction of the ice area covered by ponds.

increase in lead fraction, from 0.05 to 0.20 due to ice dynamics. The increase resulted primarily from the overall divergence of the ice pack [*Richter-Menge and Perovich*, 2001], rather than from lateral melting of the floes. The lead fraction stayed at 0.20 for the remainder of the melt season, then monotonically decreased as fall freeze-up progressed in September and October. The decrease in lead fraction primarily resulted from young ice formation, not from ice dynamic activity.

[22] The time series of A_p*, the fraction of the ice that is ponded, is intriguing. In mid-June ponds cover a few percent of the ice, but then, in just a few days, between 15 and 18 June, A_p* jumps by a factor of five from 0.04 to 0.20. After remaining at 0.20 for a few days, there is a sharp decrease to 0.15. This was followed by a steady increase for the remainder of the melt season, reaching a maximum value of 0.24 on 7 August 1998. Starting in late August, the ponds began to freeze and, by the 11 September flight, virtually all of the ponds had frozen surface layers.

[23] In a simplistic sense, we can consider the amount of water in ponds to be a balance between meltwater runoff into ponds and drainage from them. Also, the pond boundaries are not static, since they can melt on the sides and bottom. The temporal behavior of A_p* in Figure 6 can be qualitatively explained from this simple perspective. The sharp increase in pond fraction between 10 and 18 June was due to a rapid influx of water from snowmelt. There was limited drainage through the ice, as the permeability of the ice was small. There was little surface runoff to the ocean, since the network between ponds had not yet formed. We suspect that the decrease in pond area between 22 and 30 June was attributable to enhanced drainage resulting from increased ice permeability [*Eicken et al.*, 2002]. Surface-based measurements of melt ponds [*Perovich et al.*, 1999b] showed that individual ponds grew wider as the summer progressed, causing a gradual increase in the area covered by ponds from late-June through mid-August. Finally, in late-August surface melt ceased and ice formed on the surface of the melt ponds. It may be possible in the future to quantitatively describe the temporal evolution of A_p* by integrating the helicopter results with surface based measurements of heat budget, snow and ice ablation, ice porosity and permeability, and the evolution of individual ponds.

4.2. Aggregate Scale

[24] The term "aggregate scale" refers to the scale where the sampling variability of a parameter is minimized and the observed properties of the ice pack are statistically representative. Defining the state of the ice cover on the aggregate scale is needed to link small-scale process-oriented models to large-scale climate models [*Moritz et al.*, 1993]. To determine the sample size needed to achieve statistical uniformity, the standard deviations of the lead, pond, and ice fractions were determined as a function of sample area for the 15 July photography flight. These quantities were computed using each image from the 15 July flight, for the full image, and for subimages of one-half, one-quarter, one-eighth, and one-sixteenth sizes. The subimages were always selected from the upper left-hand corner of the original image. Data for groups of two to six images were also combined, averaged, and analyzed to provide larger sample areas for comparison. As Figure 7 shows, the standard deviation for all three variables decreases rapidly, gradually levels off as the sample size exceeds 1 km (approximately the areal extent of individual photographs), and slowly tapers downward as the area increases. As the standard deviation still exhibits a slow decline, even as the area approaches 6 km^2, it is likely that the standard deviation has not reached an absolute minimum and that analysis at this scale provides values that are too large by a small amount.

[25] Even though an individual image did not constitute the aggregate scale, the mean area fractions, computed by averaging the results for all photographs from a flight, provide representative values. Consider, for example, the pond fraction on 15 July; 139 photographs were analyzed, the mean pond fraction of the images was 0.188 and the standard deviation (σ) was 0.047. From the central limit theorem [*Larson*, 1969] the error of the mean is $\sigma/\sqrt{N} = 0.047/\sqrt{139} = 0.004$, or about 2% of the mean.

4.3. Pond and Floe Statistics

[26] Knowing area fractions is sufficient for estimating regional averages of albedo and of surface ablation. However, for many applications more detailed statistics on the ponds and ice floes are needed. For example, process models indicate that lateral melting depends not only on the amount of open water, but on how that open water is distributed; more floe perimeter implies more lateral melting [*Perovich*, 1983; *Maykut and Perovich*, 1987; *Perovich and Maykut*, 1990; *Steele*, 1992]. Also, statistics on pond number densities and size distributions are needed to understand, and model, the properties and evolution of melt ponds.

[27] When analyzing images to determine floe size and pond size distributions, it must be remembered that large objects are less likely to be entirely included in a photograph than small objects. More formally, the probability that a circular object of radius R, which at least touches a sample area of length (L) by width (W), will be entirely enclosed within the bounds of the sample, is given by:

$$p(R) = \frac{(L-2R)(W-2R)}{LW + 2LR + 2WR + \pi R^2} \quad (1)$$

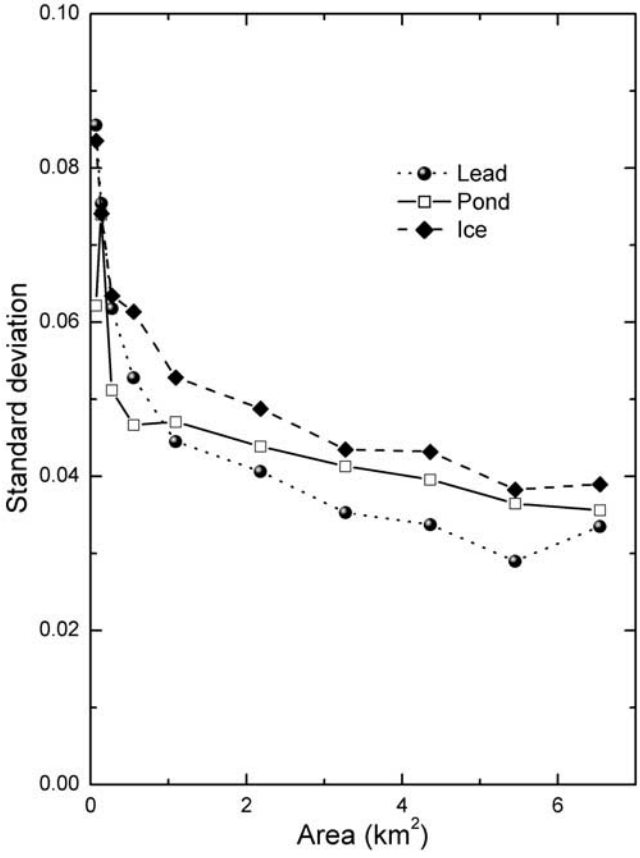

Figure 7. Standard deviation of lead, pond, and ice fraction as a function of sample area for 15 July.

There won't be any statistics for any objects where $R > W$, and the likelihood of getting accurate statistics, even for much smaller objects, drops off quickly as the size of the objects increases. Because equation (1) assumes circular objects for simplicity, it can be used only as an indicator, and not as a means for adjusting the probability density function. However, it serves as a good reminder that the number of large objects will be underestimated, and it may be used to infer some information about object inclusion probability.

[28] There are two simple methods by which the function p can be used as an indicator of object probability. The first method uses the object's measured area to calculate p for its circular counterpart. Results from this method always produce a calculated probability that is equal to or greater than the actual probability for objects that are not necessarily circular. The second method calculates p by inserting half of the calculated major axis length of an object for R in the equation. This method produces results that underestimate p.

[29] Based on the average pond sizes for each flight analyzed, and on an image size of 1280 by 855 m, the probability that a pond of mean area will appear entirely within an image ranges from 96.7% (for 7 August) to 98.4% (for 10 June). When calculations are based on major axis lengths, the probability range is from 96.2% (for 7 August) to 97.5% (for 10 June). These calculations indicate that pond statistics and size distribution can be determined reasonably well for images taken from an altitude of 1830 m (1280- $\times$ 855-m image size), but that large ponds will be somewhat underrepresented.

[30] For the pond statistics presented here, all ponds smaller than 12 pixels have been eliminated, because the resolution of the images processed cannot consistently identify objects this small. At an altitude of 1280 m, and at the high resolution of 3072 $\times$ 2048 pixels, a 12-pixel object has an area of approximately 2 m^2. The image processing software also erroneously identifies small irregularities in the ice surface as objects. By discounting objects of less than 12 pixels, these problems are minimized. It is clear from surface observations that some melt ponds were smaller than 2 m^2. However, such ponds are too small to be accurately resolved by these photographs.

[31] The areal extent of our photographs has a much greater impact on floe statistics than on pond statistics, as floes are generally much larger than ponds. On inspection of the photographs, it is clear that many floes intersect at least one border of an image. A circular object with a 37-m radius has approximately a 75% chance of falling within an image; for a object with radius 90 m, the odds fall below 50%. Such an object would be a huge melt pond, but a relatively small floe. Floes larger than this are common, and thus an accurate floe size distribution cannot be determined from these photographs. In place of a floe size distribution, floe perimeter statistics were calculated. We define floe perimeter as the sum length of all ice floe edges in an image. If a large survey area is divided into smaller samples, the sum of the floe perimeter values for each sample will equal the floe perimeter for the entire area. Floe perimeter is thus not affected by sample size, and can be used as an inferred proxy for a floe size distribution.

[32] The mean daily floe perimeter was computed by dividing the total length of perimeter measured on a flight by the total area of the images analyzed on that flight and has units of km km^{-2}. Floe perimeter changes during the melt season result from lateral melting and floe breakup. Lateral melting makes floes smaller and tends to reduce the floe perimeter, while floe breakup increases the perimeter [*Perovich*, 1983]. The time series of daily average floe perimeter and ice concentration are plotted in Figure 8.

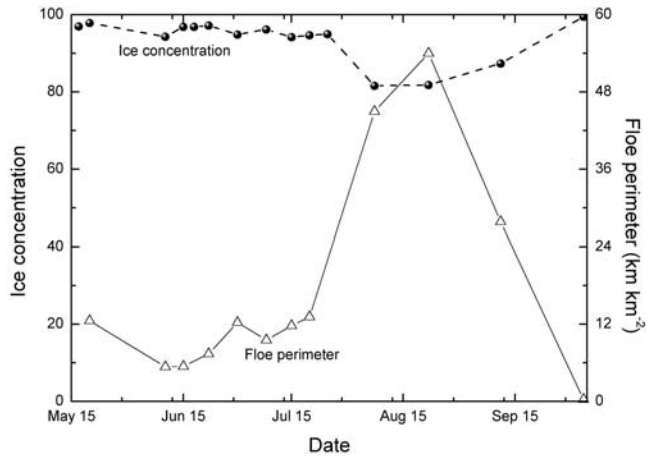

Figure 8. Time series of ice concentration and floe perimeter per unit area.

From mid-May through the end of July, the floe perimeter varied from 5 to 13 km km^{-2}. Then there was a sharp and significant increase in floe perimeter as floes fragmented during the early August divergence event. Floe perimeter decreased during fall, as freezing leads essentially erased the boundaries between individual floes.

[33] Determining lateral melting in the region surrounding SHEBA will be a complex endeavor, entailing assimilation of ice ablation, solar radiation, and upper ocean temperature and conductivity data and process modeling of ice and leads. It is possible, however, to generate a crude estimate of amount of lateral melting. Assume that the lateral melt rate was a constant 0.1 m day^{-1}, and that the upper ocean had sufficient heat to maintain this melt rate regardless of the total floe perimeter or the ice thickness. With these admittedly gross simplifications, the estimated daily change in ice concentration due to lateral melting was 0.001 on 8 July and 0.005 on 7 August. Integrating over time from 1 July through 22 August gives a total change in ice concentration attributable to lateral melt of 0.12.

[34] Figure 6 clearly shows four key inflection points in the evolution of the pond fraction: 10 June, when the melt ponds are first forming; 22 June, when ponds have spread and the pond fraction first peaks; 30 June, when the fraction is reduced by drainage, and 7 August, when the pond fraction reaches its maximum during the final stages of melt prior to freeze-up. These 4 days were selected for a statistical analysis of melt pond properties. Pond statistics were generated for every fifth image along the entire flight path for each of these days. Occasionally, complex networks of brash ice would fall within the pond threshold; adjacent photos were analyzed in place of these. For each pond in these images, area, perimeter, major axis length, major axis angle, breadth, and circularity were calculated using image-processing software [*Optimas*, 1999]. Average values of these parameters were also computed for each day, along with the pond number density. Pond number density is defined as the number of ponds divided by the area of ice and ponds, with units of ponds km^{-2}. Note that pond density is defined in terms of ice and pond area, not total area, thus eliminating effects due to changes in ice concentration. The circularity (C) is a measure of an object's shape and is defined as $C = P^2/A$, where P and A are the perimeter and area of an object.

[35] Ponds are abundant in number and diverse in shape throughout the melt season. Over 350,000 ponds were analyzed from four flights (10, 22, and 30 June and 7 August). The pond fraction varied greatly from image to image, ranging, for example, from 0.01 to 0.39 for images from 30 June. Melt pond number densities also showed considerable variation when calculated for individual images, ranging from 1826 to 4318 km^{-2} for 30 June. This results from the fact that, even at the height of the melt season, some floes have very few ponds, while others are more than 20% covered by ponds. Median pond areas for a given flight were significantly less (up to seven times less) than the mean pond areas, implying an abundance of small ponds.

[36] Values of the fraction of ice covered by ponds (A_p*) are plotted in Figure 9a. The data show an initial peak of 0.193 on 22 June, followed by a decrease to 0.126 on 30 June, rising to a final peak of 0.247 on 7 August before the commencement of fall freeze-up (Table 2). The small differences between the average values of A_p* reported in Tables 1 and 2 for these days are attributable to the analysis of fewer photographs at a higher resolution for Table 2.

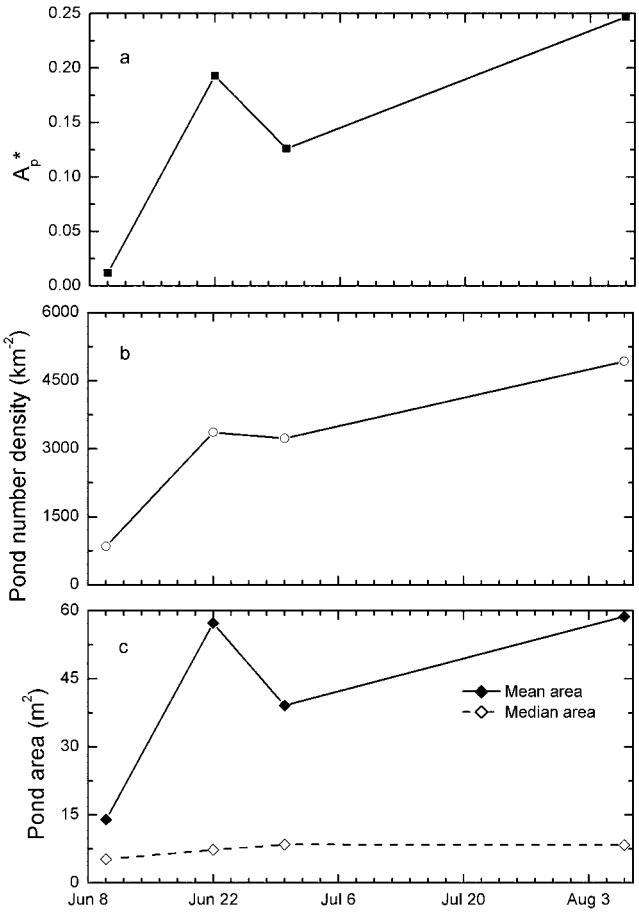

Figure 9. Statistical description of melt ponds for 10, 22, and 30 June, and 7 August: (a) fraction of ice area covered by ponds (A_p*), (b) melt pond number density, and (c) mean and median pond area. The pond number density is the number of melt ponds per square kilometer of ice.

[37] Melt pond number density (Figure 9b) increased by a factor of four from 10 to 22 June, as pond coverage rapidly increased. This was followed by a slight decrease in number density on 30 June as A_p* decreased sharply by one-third. The decline in pond number density from 22 to 30 June is relatively less than the decrease in pond fraction for these dates. Visual observations and pond statistics indicate a significant decrease in pond size between these 2 days. Mean pond area decreased from 57.3 to 39.1 m^2 (Figure 9c) and the average pond perimeter for this interval dropped from 34.2 to 30.8 m. Interestingly, there was a slight increase in median pond area from 7.3 to 8.5 m^2 between 22 and 30 June. These data suggest that the drop in pond surface coverage was due more to pond shrinkage, than to a simple decrease in pond number. Melt pond evolution is discussed in detail by *Eicken et al.* [2002].

[38] As can be seen in Figures 2, 3, and 12, melt ponds vary considerably in shape, from simple ovals to intricate interconnected structures. One measure of an object's shape

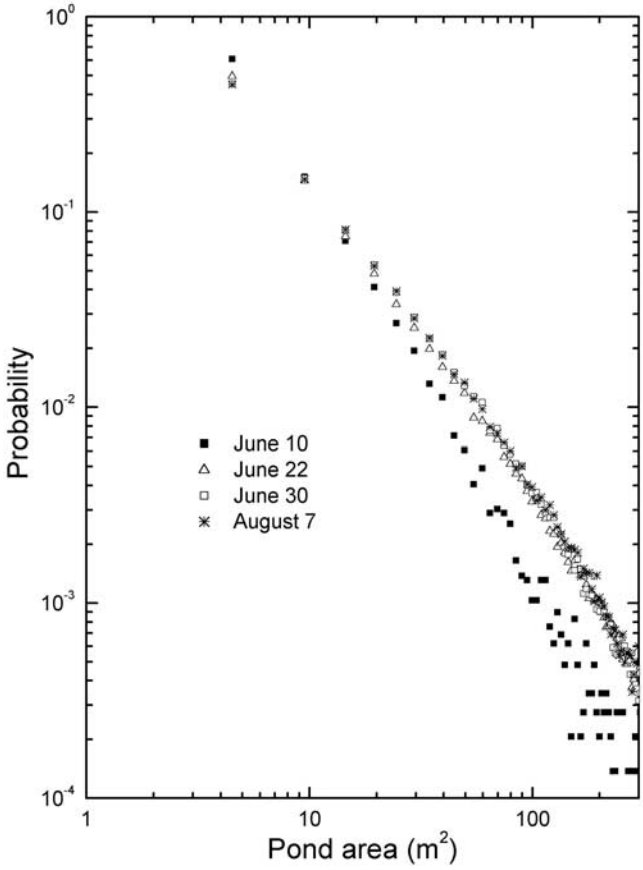

Figure 10. Melt pond size distributions for 10, 22, and 30 June and 7 August. Area bins of 5 m^2 were used.

is the circularity. The smallest possible value of circularity is for a circle ($C = 4\pi$). As the shape becomes more intricate, the circularity increases. The mean circularity for ponds ranged from 38.5 on 10 June to 41.2 on 7 August. For comparison, a 1:8 rectangle has a circularity of 40.5. These values reaffirm the presence of many noncircular, geometrically complex ponds and indicate that, on average, there was a slight increase in the geometric complexity of the ponds as A_p* and pond area increased.

[39] As we have mentioned before, ponds were ubiquitous during the melt season. Even for the 10 June flight, at the beginning of the melt season, we analyzed over 10,000 ponds. After computing pond density and area statistics, we generated size distribution histograms, binned at 5 m^2 intervals. Pond size distributions for all four flights are shown in Figure 10. This figure, graphed on log-log axes, clearly illustrates the predominance of small ponds, as is also demonstrated by the difference between their mean and median areas (Table 2). It also shows that the pond size distributions are of a similar form for the four flights analyzed. Only 10 June, at the beginning of the melt season, displays a noticeably different distribution. Data for this date also demonstrate some scattering at the high end of the distribution, owing in part to the early stage of the melt season, and the fewer number of ponds for 10 June.

[40] We expect that the values of pond statistics would vary by location and by year, but that the general trends observed would not change. To facilitate comparisons between pond statistics on different days and to generalize the pond size distribution throughout the melt season for modeling applications, we applied curve-fitting software to the data [*Jandel Scientific*, 1998]. As the linear dependence of the data in the log-log plot in Figure 9 indicate, pond size distributions for all four flights are well fit by a power law. The form of the relationship is

$$P(A) = aA^b \tag{2}$$

where $P(A)$ is the probability density function, A is the pond area, and a and b are coefficients (Table 2). The fit is excellent, with correlation coefficients greater than 0.999. Note that probability decreases as pond size increases and the exponent b is negative. For 30 June and 7 August, the exponent is approximately $-3/2$. The cumulative probability distribution is the integral of equation (2) and for these cases is

$$CDF(A) = \frac{-2a}{\sqrt{A}}\Big]_2^{\infty}.$$

Perovich and Tucker [1997] determined that pond size was well fit (R^2 = 0.999) by a two-parameter cumulative lognormal distribution of the form

$$CDF(A)\frac{1}{2}erfc\left[\frac{-(\ln A - \ln \mu)}{\sigma\sqrt{2}}\right] \tag{3}$$

where μ and σ are the mean and standard deviation of the variable $\ln(A)$. For each flight, equation (3) was used to fit the cumulative distribution of ponds of size 2 to 1000 m. Results are summarized in Table 2. The fit (R^2 0.96 to 0.99)

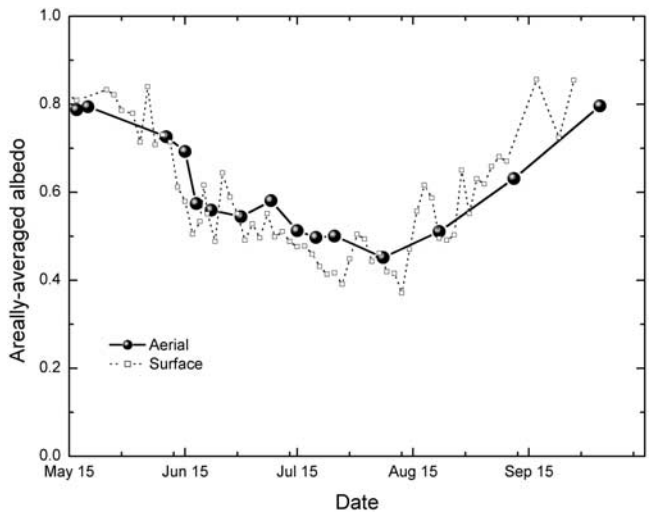

Figure 11. Time series of areally averaged albedo determined from aerial observations of area fractions and surface based albedo measurements. The estimated albedo for the 50 × 50 km region around SHEBA (solid line, spheres) is plotted. For comparison, albedos measured on the surface along a 200-m-long line (dotted line, open squares) from *Perovich et al.* [2002] are also plotted.

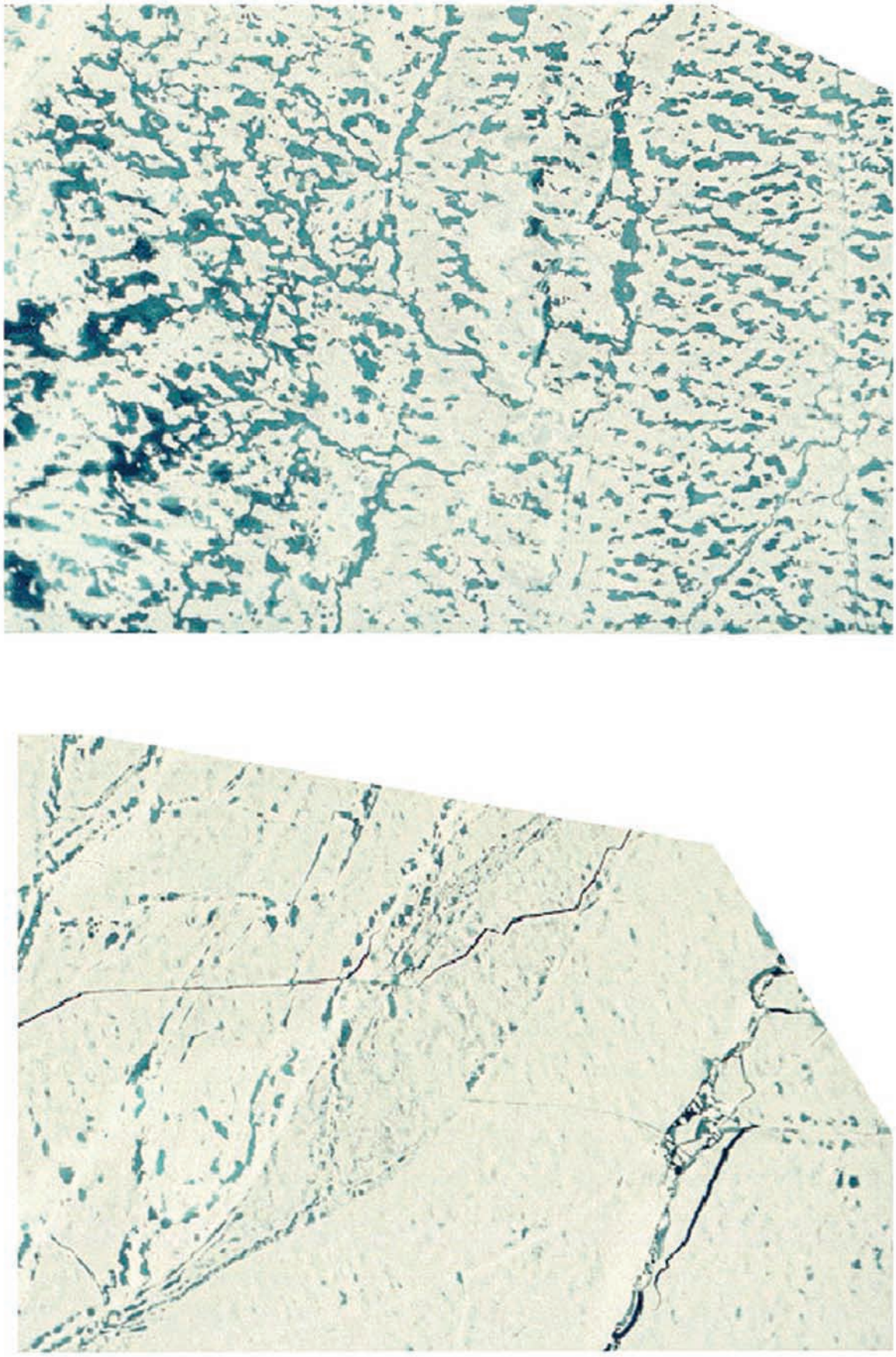

Figure 12. Photographs of melt ponds on first-year ice (a) heavily ponded and (b) unponded. Both photographs were taken on 15 July.

was not as good as found by *Perovich and Tucker* [1997], or as good as the fit for equation (2). For all four flights, equation (3) overestimated the number of small ponds.

5. Discussion

[41] As was stated earlier, a major goal of the SHEBA program is to understand the ice-albedo feedback. Combining the area fraction data with surface-based measurements of albedo [*Perovich et al.*, 2002], we can estimate the evolution of albedo on the scale of a single column model ($\sim$50 $\times$ 50 km) by weighting surface-based albedos of the constituent surface components (ice, ponds, young ice, and leads) by their area fractions. This is expressed as

$$\overline{\alpha} = \alpha_i A_i + \alpha_p A_p + \alpha_y A_y + \alpha_w A_w,$$

where $\overline{\alpha}$ is the areally averaged albedo, α is the albedo, A is the area fraction and the subscripts denote snow or ice (i), ponds (p), young ice (y), and open water (w). Input data for this equation are summarized in Table 3. This is a simplification, as it assumes that there are only four possible surface states and that each state can be represented by a single albedo. Surface observations have established that bare ice (α_i) and lead albedos (α_w) show little variability [*Pegau and Paulson*, 1999; *Perovich et al.*, 2002]. However, albedos do vary from pond to pond [*Grenfell and Maykut*, 1977; *Perovich et al.*, 2002], so an average of a light pond and dark pond for was used for α_p. Young ice albedos are sensitive to ice thickness and the value of α_y appropriate for the presumed average thickness of the young ice was used.

[42] The areally averaged albedo plotted in Figure 11 (solid line, spheres) displays a smooth seasonal dependence and follows the five-phase evolutionary form suggested by *Perovich et al.* [2002]. For comparison, average daily albedos measured on the surface along a 200-m-long line (dotted line, open squares) from *Perovich et al.* [2002] are also plotted. There is good agreement in the temporal behavior between the surface measurements and the areal estimates. The magnitudes do not agree precisely, since the surface albedo did not include leads and had a higher pond fraction than the overall ice cover. The albedo is near 0.8 in May before melt has begun and when the open water fraction was only a few percent. There is a decrease in early June as the snow begins to melt, followed by a sharp drop in mid-June, associated with the rapid increase in pond fraction. This is followed by a gradual decrease for the remainder of the summer as the pond fraction increases. The slight increase in albedo on 8 July was due to a decrease in the lead fraction caused by a modest convergence of the ice pack. Finally, after mid-August, the areally averaged albedos monotonically increased as the ponds and leads froze.

[43] Our qualitative observations of melt ponds on first-year ice agreed, in part, with observations by other researchers [*Holt and Digby*, 1985; *Derksen et al.*, 1997; *Naggar et al.*, 1998; *Fetterer and Untersteiner*, 1998] who found that first-year ice pond fractions typically were large and greater than on multiyear ice. We saw first-year floes with pond fractions greater than 50% (Figure 12a). However, we also observed areas of first-year ice, at the height of the melt season, with few, if any, melt ponds (Figure 12b). On two occasions we were able to land on such floes and make ice thickness and salinity measurements. From these measurements we determined that the floes were first-year ice. It appears that first-year ice may have two potential pond paths: one where it becomes heavily ponded and one almost unponded. At this stage, we know neither the cause of the differences nor the relative frequency of these two paths. These questions can be addressed by integrating results from surface-based studies of melt ponds and ice properties [*Perovich et al.*, 1999b] with further analysis of the images.

[44] The helicopter photographs can be further analyzed and interpreted. We can revisit the helicopter photographs to determine pond statistics for individual floes [*Fetterer and Untersteiner*, 1998] and to investigate differences attributable to floe size or between first-year and multiyear ice. Such results could be incorporated into large-scale sea ice models, which typically treat first-year and multiyear ice separately.

[45] A rich data set of imagery is available for Ice Station SHEBA from the SHEBA field year (October 1997 through October 1998). In addition to the helicopter photographs discussed in this paper and the low altitude video presented by *Tschudi et al.* [2001], there are extensive remote sensing data for SHEBA, including approximately 60 black and white reconnaissance images of the SHEBA area [*National Snow and Ice Data Center*, 2000], as well as a complete set of Radarsat images. These varied data sources both supplement and complement one another. The helicopter photographs give the greatest detail and color information, but there are only 14 flights between mid-May and October 1998. The black and white reconnaissance images have less spatial resolution, but greater spatial and temporal coverage, though they have no coverage during the Arctic night. The Radarsat images have the poorest spatial resolution, but the largest areal coverage and the most complete time series. The data sets are synergistic and a combined analysis would be productive. For example, they could be combined to determine the floe size distribution. The sizes of small floes can be determined from the aerial photographs, intermediate sizes from reconnaissance images, and the largest floes from Radarsat images. Since there is overlap between the different spatial scales of the images, it is possible to combine results to determine the floe size distribution. A time series of such distributions could be analyzed to ascertain the relative importance of lateral melting and floe breaking. It could also be used to initiate and evaluate discrete element models of the summer ice cover.

6. Summary

[46] The Arctic sea ice cover undergoes a dramatic change in surface conditions in response to summer melt. The surface changes from a homogeneous highly reflective surface to a heterogeneous mixture of bare ice, melt ponds, and leads, with an albedo that is significantly smaller. The key factors contributing to this reduction in albedo are the melting of the snow cover, the formation and growth of the melt ponds, and the increase in the open water fraction. Changes in surface conditions on a scale of 50 $\times$ 50 km were documented by analyzing aerial photographs

from helicopter survey flights flown between 20 May and 4 October 1998. Estimates of areally averaged albedo show a seasonal evolution similar to that reported by *Perovich et al.* [2002]. The maximum estimated albedo of 0.80 was before melt in May and after freeze-up in October, while the minimum estimated albedo of 0.45 was on 7 August, the height of the melt season.

[47] Summer changes in pond and lead fraction are a combination of continuous evolution and discrete changes. Shortly after the first appearance of melt ponds in early June, there was a discrete jump in pond coverage from 0.05 to 0.20 between 15 and 18 June. After approximately 7–10 days, there was a discrete drop in pond fractions. For the remainder of the summer there was a steady and gradual increase in pond fraction as the ponds evolved. The peak pond coverage at the height of the melt season in early August exceeded 0.2. By mid-September the surface of virtually all of the ponds had frozen. Melt ponds were ubiquitous during summer, with number densities increasing from 1000 to 5000 ponds km^{-2} between June and August. Small ponds were much more common than large ponds and the pond size distribution can be represented by a power law with a negative exponent.

[48] Lead fraction varied unsystematically between 0.02 and 0.05 from May through the end of July. This was followed by a discrete jump to 0.20 in early August due to ice divergence. Associated with this increase in lead fraction was an increase in the floe perimeter. As the ice pack diverged, the thermally weakened ice floes broke apart, increasing the number of floes and increasing the floe perimeter.

[49] **Acknowledgments.** Special thanks to T.C. Grenfell and B. Light for their excellent contributions preparing for and participating in the helicopter photography flights. We deeply appreciate the support of the pilots, helicopter mechanics, and crew of the *Des Groseilliers* who professionally executed these flights. We also thank J.A. Richter-Menge, H. Eicken, B. Elder, and H. Bosworth for their assistance in acquiring the photographs and K. Claffey, V. Fusca, and N. Perron for their efforts in analyzing the images. This work was funded as part of the National Science Foundation, Office of Naval Research SHEBA program under the ONR high-latitude program.

References

Barry, R. G., The parameterization of surface albedo for sea ice and it snow cover, *Prog. Phys. Geogr.*, *20*, 61–77, 1996.

Barry, R. G., M. C. Serreze, J. A. Maslanik, and R. H. Preller, The Arctic sea ice-climate system: Observations and modeling, *Rev. Geophys.*, *31*, 397–422, 1993.

Briegleb, B. P., and D. H. Bromwich, Polar radiation budgets of NCAR CCM3, *J. Clim.*, *11*, 1246–1269, 1998.

Carsey, F. D., Summer Arctic sea ice character from satellite microwave data, *J. Geophys. Res.*, *90*, 5015–5034, 1985.

Curry, J. A., J. L. Schramm, D. K. Perovich, and J. O. Pinto, Applications of SHEBA/FIRE data to evaluation of snow/ice albedo parameterizations, *J. Geophys. Res.*, *107*, 10.1029/2000JC000466, in press, 2002.

Derksen, C., J. Piwowar, and E. LeDrew, Sea ice melt pond fraction as determined from low level aerial photographs, *Arct. Alp. Res.*, *29*, 345–351, 1997.

Eicken, H., R. Gradinger, B. Ivanov, A. Makshtas, and R. Pac, Surface melt puddles on multi-year sea ice in the Eurasian Arctic, in *Proceedings of the ACSYS Conference on the Dynamics of the Arctic Climate System*, pp. 267–271, World Clim. Res. Programme WCRP-94, Goteburg, Sweden, 1994.

Eicken, H., R. Krouse, D. Kadko, and K. Perovich, Tracer studies of pathways and rates of meltwater transport through Arctic summer sea ice, *J. Geophys. Res.*, *107*, 10.1029/2000JC000583, in press, 2002.

Fetterer, F., and N. Untersteiner, Observations of melt ponds on Arctic sea ice, *J. Geophys. Res.*, *103*, 24,821–24,835, 1998.

Grenfell, T. C., and G. A. Maykut, The optical properties of ice and snow in the Arctic Basin, *J. Glaciol.*, *18*, 445–463, 1977.

Grenfell, T. C., and D. K. Perovich, Spectral albedos of sea ice and incident solar irradiance in the Southern Beaufort Sea, *J. Geophys. Res.*, *89*, 3573–3580, 1984.

Hanson, A., Studies of the mass budget of arctic pack ice, *J. Glaciol.*, *5*, 701–709, 1965.

Holt, B., and S. A. Digby, Processes and imagery of first-year fast sea ice during the melt season, *J. Geophys. Res.*, *90*, 5045–5062, 1985.

Ingram, W. J., C. A. Wilson, and J. F. B. Mitchell, Modeling climate change: An assessment of sea ice and surface albedo feedbacks, *J. Geophys. Res.*, *94*, 8609–8622, 1989.

Jandel Scientific, *Table Curve User's Manual*, Jandell Scientific, San Raphael, Calif., 1998.

Langleben, M. P., Albedo of melting sea ice in the southern Beaufort Sea, *J. Glaciol.*, *8*, 407–412, 1969.

Larson, H. J., *Introduction to Probability Theory and Statistical Inference*, 387 pp., John Wiley, New York, 1969.

Lindsay, R. W., and D. A. Rothrock, Arctic sea ice albedo from AVHRR, *J. Clim.*, *7*, 1737–1749, 1994.

Manabe, S., and R. J. Stouffer, Century-scale effects of increased atmospheric CO_2 on the ocean-atmosphere system, *Nature*, *364*, 215–218, 1993.

Manabe, S., R. J. Stouffer, M. J. Spelman, and K. Bryan, Transient response of a couple ocean-atmosphere model to gradual changes of atmospheric CO_2, part I, Annual mean response, *J. Clim.*, *4*, 785–817, 1991.

Maykut, G. A., and M. G. McPhee, Solar heating of the arctic mixed layer, *J. Geophys. Res.*, *100*, 24,691–24,703, 1995.

Maykut, G. A., and D. K. Perovich, On the role of shortwave radiation in the summer decay of a sea ice cover, *J. Geophys. Res.*, *92*, 7032–7044, 1987.

McPhee, M., T. Stanton, J. Morison, and D. Martinson, Freshening of the upper ocean in the Central Arctic: Is perennial sea ice disappearing, *Geophys. Res. Lett.*, 1998.

Moritz, R. E., and D. K. Perovich, (Eds.), *Surface Heat Budget of the Arctic Ocean, Science Plan, ARCSS/OAII Rep. 5*, 64 pp., Univ. of Wash., Seattle, Wash., 1996.

Moritz, R. E., J. A. Curry, A. S. Thorndike, and N. Untersteiner, *SHEBA a Research Program on the Surface Heat Budget of the Arctic Ocean, Rep. 3*, 34 pp., Arctic Syst. Sci.: Ocean-Atmos.-Ice Interact., 1993.

Naggar, S. El, C. Garrity, and R. O. Ramseier, The modeling of sea ice melt-water ponds for the High Arctic using an airborne line scan camera, and applied to the Satellite Special Sensor Microwave/Imager (SSM/I), *Int. J. Remote Sens.*, *19*, 2373–2394, 1998.

National Snow and Ice Data Center. SHEBA Reconnaissance Imagery Version 1.0, ARCSS Data Coord. Center, Univ. of Colo., Boulder, Colo., 2000.

Nazintsev, Y. L., The heat balance of the surface of the multiyear ice cover in the central Arctic (in Russian), *Tr. Arkt. Antarkt. Nauchno-Issled. Inst.*, 110–126, 1964.

Optimas, *Optimas 6.5, User Guide and Technical Reference*, Optimas, Seattle, Wash., 1999.

Pegau, W. S., and C. A. Paulson, The effects of clouds on the albedo of Arctic leads, *Eos Trans. AGU*, *80*, F221, 1999.

Perovich, D. K., On the summer decay of a sea ice cover, Ph.D. thesis, Univ. of Wash., Seattle, Wash., 1983.

Perovich, D. K., and G. A. Maykut, The treatment of shortwave radiation and open water in large-scale models of sea ice decay, *Ann. Glaciol.*, *14*, 242–246, 1990.

Perovich, D. K., and W. B. Tucker III, Arctic sea ice conditions and the distribution of solar radiation during summer, *Ann. Glaciol.*, *25*, 445–450, 1997.

Perovich, D. K., et al., Year on ice gives climate insights, *Eos Trans. AGU*, *80*(481), 485–486, 1999a.

Perovich, D. K., T. C. Grenfell, B. Light, J. A. Richter-Menge, M. Sturm, W. B. Tucker, III, H. Eicken, G. A. Maykut, and B. Elder, *SHEBA: Snow and Ice Studies* CD-ROM, October, 1999b.

Perovich, D., C. Grenfell, B. Light, and V. Hobbs, Seasonal evolution of the albedo of multiyear Arctic sea ice, *J. Geophys. Res.*, *107*, 10.1029/2000JC000438, in press, 2002.

Richter-Menge, J. A., and D. K. Perovich, Temporal evolution of Arctic sea ice temperature, *Ann. Glaciol.*, *33*, 207–211, 2001.

Rind, D., R. Healy, C. Parkinson, and D. Martinson, The role of sea ice in 2 $\times$ CO_2 climate model sensitivity, part I, the total influence of sea ice thickness and extent, *J. Clim.*, *8*, 449–463, 1995.

Rothrock, D. A., and A. S. Thorndike, Measuring the sea ice floe size distribution, *J. Geophys. Res*, *89*, 6477–6486, 1984.

Steele, M., Sea ice melting and floe geometry in a simple ice-ocean model, *J. Geophys. Res.*, *97*, 17,729–17,738, 1992.

Tschudi, M. A., J. A. Curry, and J. A. Maslanik, Determination of areal

surface-feature coverage in the Beaufort Sea using aircraft video data, *Ann. Glaciol.*, *25*, 434–438, 1997.

Tschudi, M. A., J. A. Curry, and J. A. Maslanik, Airborne observations of summertime surface features and their effect on surface albedo during SHEBA, *J. Geophys. Res.*, *106*(D14), 10.1029/2000JD900275, 2001.

Tucker, W. B., III, A. J. Gow, D. A. Meese, and H. W. Bosworth, Physical characteristics of summer sea ice across the Arctic Ocean, *J. Geophys. Res*, *104*, 1489–1504, 1999.

Untersteiner, N., On the mass and heat budget of Arctic sea ice, *Arch. Meteorol., Geophys. Bioklimatol., Ser. A*, *12*, 151–182, 1961.

Zubov, N. N., *Arctic Ice* (in Russian) 491 pp., Istatel'stvo Glasevmorputi, Moscow, 1945.

K. A. Ligett, D. K. Perovich, and W. B. Tucker III, Engineer Research and Development Center–Cold Regions Research and Engineering Laboratory, 72 Lyme Road, Hanover, NH 03755, USA. (perovich@crrel.usace.army.mil)